Supplementary Material for: Cretaceous Oceanic Anoxic Events prolonged by phosphorus cycle feedbacks

Sebastian Beil[1], Wolfgang Kuhnt[1], Ann Holbourn[1], Florian Scholz[2], Julian Oxmann[2], Klaus Wallmann[2], Janne Lorenzen[3], Mohamed Aquit[4], El Hassane Chellai[5]

[1]Institute of Geosciences, Christian-Albrechts-University, Ludewig-Meyn-Str. 10-14, D-24118 Kiel, Germany
[2]Geomar Helmholtz Centre for Ocean Research Kiel, Wischhofstr. 1-3, D-24148 Kiel, Germany
[3]Janne Lorenzen, Christian-Albrechts-University, Ludewig-Meyn-Str. 10-14, D-24118 Kiel, Germany
[4]OCP S.A., Direction de Recherche et Développement, Recherche Géologique, 46300 Youssoufia, Morocco
[5]Department of Geology, Faculty of Sciences Semlalia, Cadi Ayyad University, Marrakech, Morocco

Correspondence to: Sebastian Beil (Sebastian.Beil@ifg.uni-kiel.de) or Wolfgang Kuhnt (Wolfgang.Kuhnt@ifg.uni-kiel.de)

Supplementary Material S1 -Phosphorus species in marine sediments

A variety of phosphorus species are discriminated including detrital phosphorus (P_{detr}), authigenic phosphorus (P_{auth}), aluminium and iron bound phosphorus ($P_{Al/Fe}$), and organic bound phosphorus (P_{org}). Detrital phosphorus (P_{detr}) is passively transported as fluviatile sediment load and is regarded as not bio-available due to its inert nature. Phosphorus adhesively bound to iron- or aluminium-crusts ($P_{Al/Fe}$) constitutes an important sink for phosphorus in marine sediments. Early diagenetic conversion of ($P_{Al/Fe}$) via biochemical process can convert this pool to authigenic phosphorus (Jarvis et al., 1994). Authigenic phosphorus (P_{auth}) mainly consists of authigenic apatite (calcium-fluor-apatite, CFA) which precipitates during early diagenesis and is typically enriched in organic-rich sediments of coastal upwelling systems (Ruttenberg, 1993). The two main sources for CFA are microbial remineralization of organic material or remobilization (e.g., during changes of the redox environment towards low-oxygen conditions) of phosphorus bound to iron-oxyhydroxides (Jarvis et al., 1994) during "sink switching" (Ruttenberg and Berner, 1993; Ruttenberg, 1993; Slomp et al., 1996a, b). CFA constitutes the main component extracted as CaP with the CONVEX method (Oxmann et al., 2008). In contrast to organic phosphorus or phosphorus bound to Al-/Fe-oxyhydroxides, CFA is a permanent sink for reactive phosphorus (Ruttenberg, 2003).

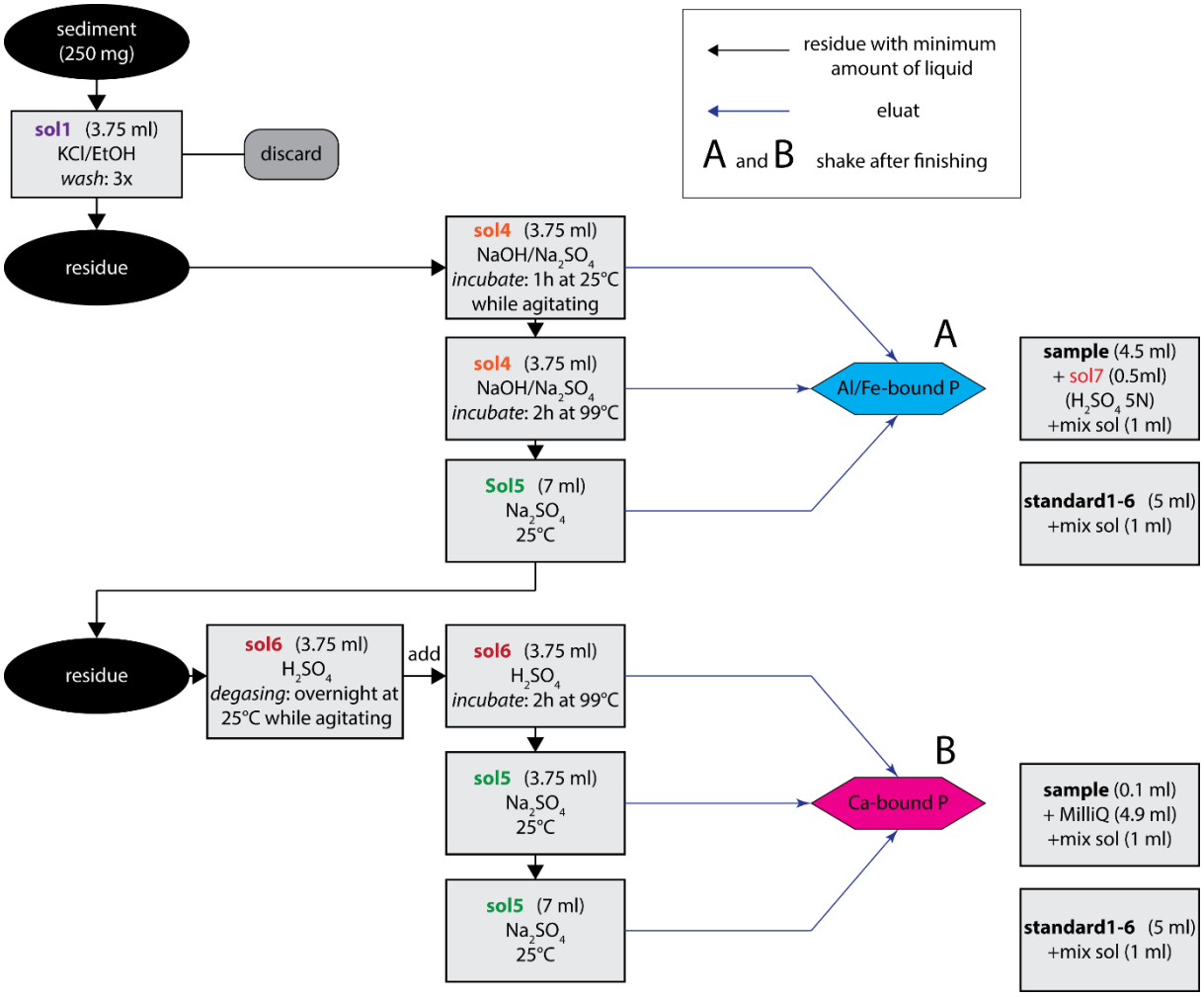

Fig. S2. Modified version of the CONVEX extraction method of Oxmann et al. (2008) used for the determination of phosphorus speciation in Core SN°4. Sol1-6 refers to different chemical solutions presented in Table S3.

Table S3 - Chemical solutions for the CONVEX extraction method of Oxmann et al. (2008).

Solution 1 – KCl 1N

Dry KCl at 110°C for 2h

Dissolve dry KCl	in H_2O (MilliQ)	add etilic alcohol
14.912 g	200 ml	300 ml
29.824 g	400 ml	600 ml
37.28 g	500 ml	750 ml

Solution 2 – NaOH 2N

Dissolve NaOH	in H_2O (MilliQ)
8 g	100 ml
40 g	0.5 l
80 g	1 l

Solutions 3 – Na_2SO_4 2N

Dissolve Na_2SO_4	in H_2O (MilliQ)
14.2 g	100 ml
71 g	0.5 l
142 g	1 l

Solution 4 – (Sol2 + Sol3)

NaOH (Sol2)	and	Na_2SO_4 (Sol3)
50%	+	50%

Solution 5 – Na_2SO_4 4%

Dissolve Na_2SO_4	in H_2O (MilliQ)
40 g	1 l
80 g	2 l

Solutions 6 – H_2SO_4 1N

Dilute H_2SO_4	in H_2O (MilliQ)
27 ml	1 l

Solution 7 – H_2SO_4 5N

Dilute H_2SO_4	in H_2O (MilliQ)
135 ml	1 l

Supplementary Material S4 - Photometric solution and standards used for measurement of the phosphorus species extracted with a modified version of the CONVEX extraction scheme of Oxmann et al. (2008).

Mix-solution

1. 4.9N Sulphuric acid
   (1) Ca. 500 ml MilliQ into 1l-flask
   (2) Add 136 ml conc. H_2SO_4 (95-97%) (corrosive!)
   (3) Fill up to 1000 ml MilliQ
2. Ammonium molybdate solution
   (use plastic spatula!)
   (1) Dissolve 10 g ammonium heptamolybdate tetrahydrate (harmful!)
   (2) Fill up to 250 ml with MilliQ

   Solution is stable for 2 weeks.

   Discard if a blue colour occurs.
3. Ascorbic acid solutions
   (1) Dissolve 4.5 g L-ascorbin-acid in MilliQ in 250 ml flask
   (2) Fill up to 250 ml with MilliQ

   Solution is stable for 1 week.

   Store cool and in darkness.
4. Potassium antimony tartrate solution
   (1) Dissolve 1.25 g Potassium antimony-(III)-oxitartrate hemihydrate (toxic) in MilliQ in 500 ml flask with magnetic stirrer on heating plate
   (2) Fill up to 500 ml with MilliQ

   Solution is stable for 1 month.

Mixed reagent: For	**20 ml**	**40 ml**	**50 ml**	**100 ml**	**120 ml**
4.9N H_2SO_4	10 ml	20 ml	25 ml	50 ml	60 ml
Ammonium molybdate solution	3 ml	6 ml	7.5 ml	15 ml	18 ml
Ascorbic acid solution	6 ml	12 ml	15 ml	30 ml	36 ml
Potassium antimony tartrate solution	1 ml	2 ml	2.5 ml	5 ml	6 ml

Solution is stable for only 12 hours!

Standards

Standard-solution

1. 5 ml Merck standard (1000 mg PO_4/l) into 1l flask
2. Fill up with MilliQ → 5 mg PO_4/l

Standards

Std#	**concentration**	**Standard-solution**	**MilliQ**	**Total Volume**

1	0	0 µl	5000 µl	5 ml
2	1%	50 µl	4950 µl	5 ml
3	5%	250 µl	4750 µl	5 ml
4	10%	500 µl	4500 µl	5 ml
5	50%	2500 µl	2500 µl	5 ml
6	75%	3750 µl	1250 µl	5 ml

Add 1 ml mix solution to 5 ml standards or 5 ml samples

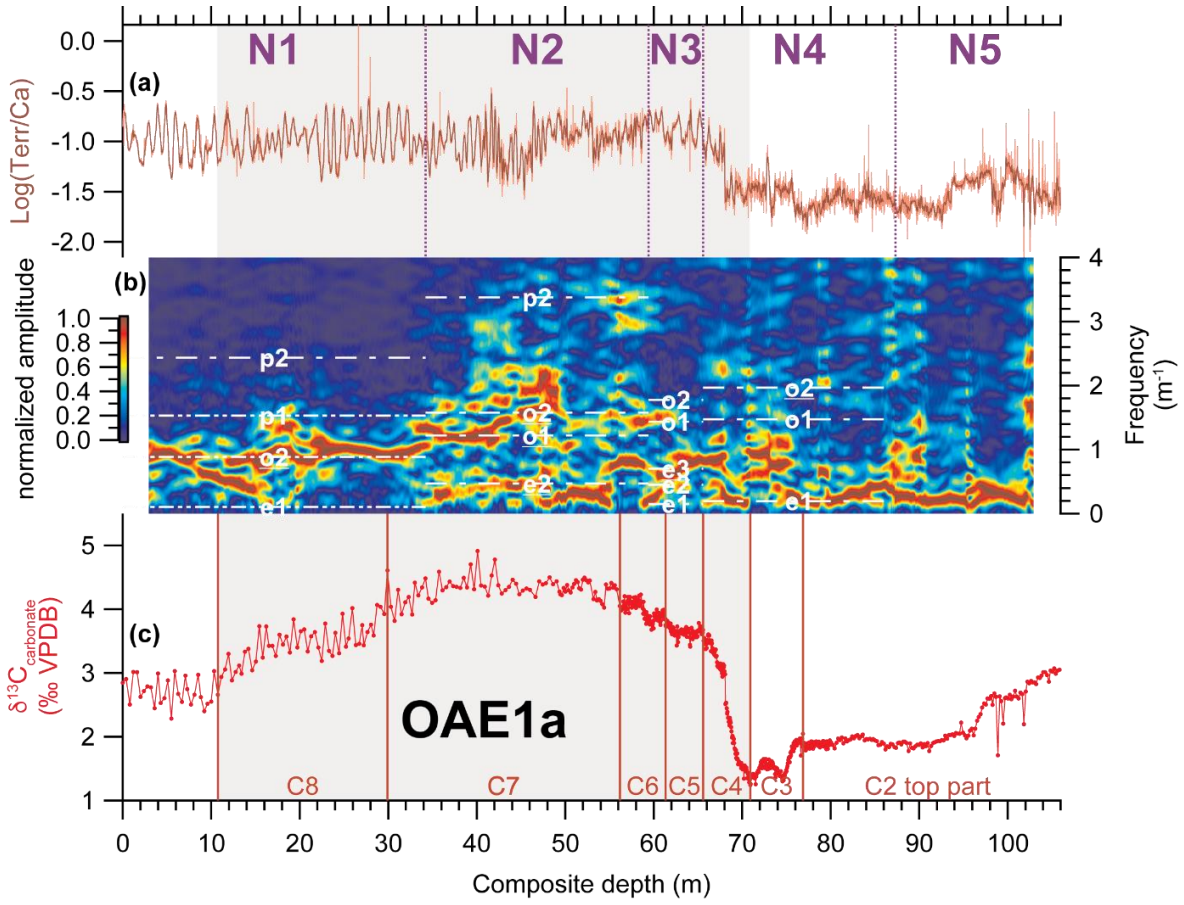

Fig. S5. Evolutive Harmonic Analysis (normalized amplitude) of XRF-derived Log(Terr/Ca) from Core LB3LB1. **(a)** XRF-scanning derived Log(Terr/Ca). **(b)** EHA diagram of Log(Terr/Ca). **(c)** $\delta^{13}C_{carbonate}$ from Lorenzen et al. (2013) for LB1 with new high-resolution isotope data from this study and from Moullade et al. (2015) for LB3. Dashed vertical lines in purple indicate segments used for power spectrum analysis of the NGR-record. Carbon isotope stages of Menegatti et al. (1998) are represented by vertical red lines with numbering at the bottom.

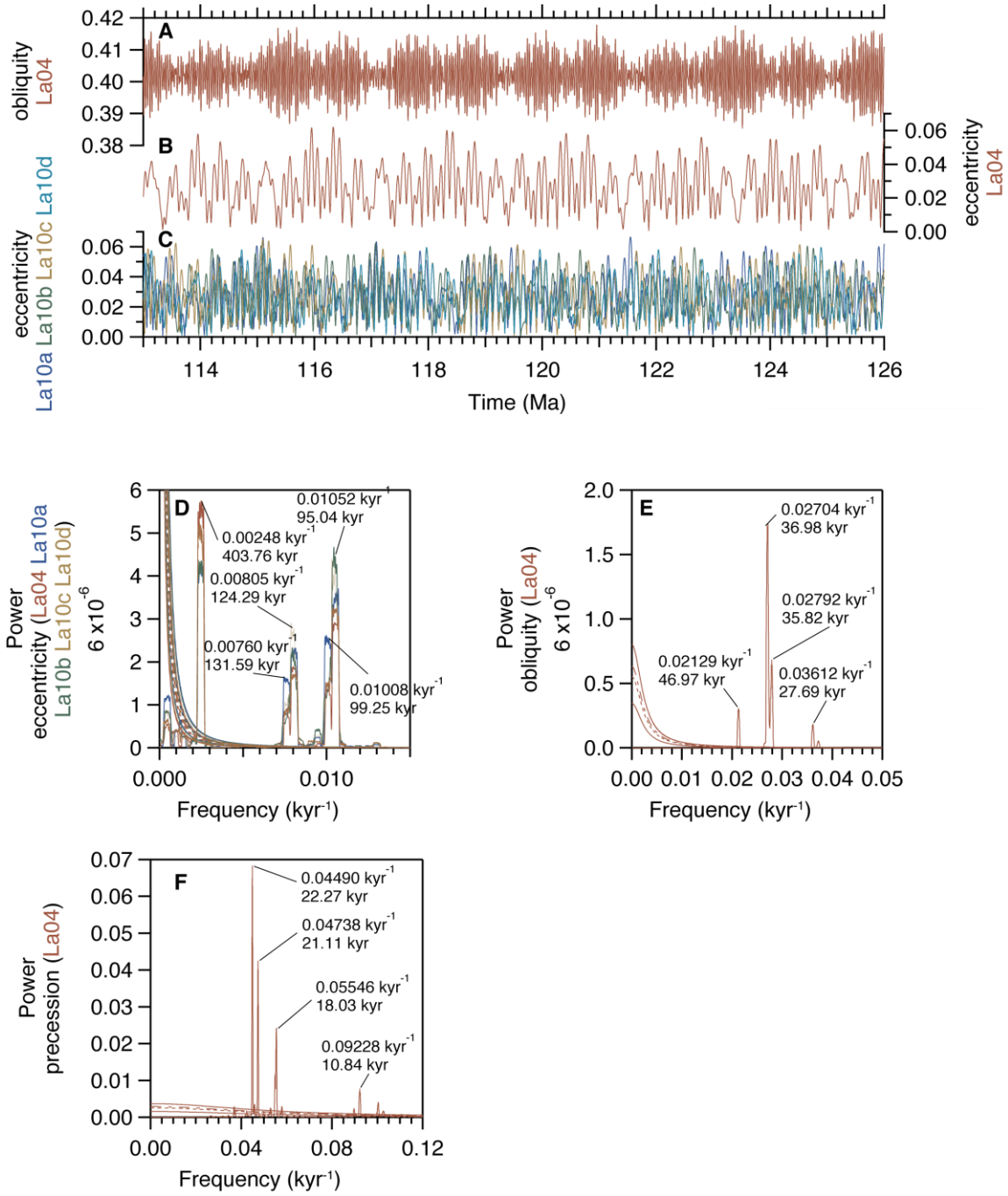

90 **Fig. S6.** Orbital Solutions for the Aptian interval between 113 and 126 Ma from Laskar et al. (2004, 2011a). **(a)** Obliquity from Laskar et al. (2004). **(b)** Eccentricity from Laskar et al. (2004). **(c)** Eccentricity from Laskar et al. (2011a). **(d)** Power spectra for eccentric from Laskar et al. (2004, 2011a). **(e)** Power spectrum for obliquity from Laskar et al. (2004). **(f)** Power spectrum for precession from Laskar et al. (2004).

Table S7. Identified orbital frequencies and ratios for the Aptian from Laskar et al. (2004, 2011a).

orbital cycle		frequency (kyr^{-1})	duration (kyr)	ratio (normalized to e1)
eccentricity	e1	0.002477	403.76	1
	e2	0.008045	124.29	3.25
	e3	0.010522	95.04	4.25
obliquity	o1	0.02129	46.97	8.60
	o2	0.027044	36.98	10.92
precession	p1	0.044904	22.27	18.13
	p2	0.055456	18.03	22.39

Table S8. Identified orbital frequencies and ratios for the Cenomanian from Laskar et al. (2004, 2011a, 2011b).

orbital cycle		frequency (kyr^{-1})	duration (kyr)	ratio (normalized to e1)
eccentricity	e1	0.00246617	405.49	1
	e2	0.00786509	127.14	3.19
	e3	0.0103313	96.79	4.19
obliquity	o1	0.0207292	48.24	8.41
	o2	0.0265614	37.65	10.77
	(o2)			
	(o3)	0.0356262	28.07	14.45
precession	p1	0.0445244	22.46	18.05
	p2	0.0545558	18.33	22.12
	p3	0.091148	10.97	36.96

Supplementary Material S9 - Subdivisions of the $\delta^{13}C$ records of OAE2 and 1a

The background level of $\delta^{13}C_{org}$ in the Tarfaya Basin in Core SN°4 (Fig. 2) is -28.5 ±0.3 ‰ in the interval preceding the precursor phase between 189.65 and 115.57 m. The precursor phase (between 115.57 and 107.14 m) shows two prominent troughs with minima of -28.8 ‰ at 111.46 and 107.14 m which are preceded by two less pronounced $\delta^{13}C_{org}$ minima at 113.55 and 115.15 m. The onset phase (between 107.14 and 103.22 m) is characterized by a strong increase in $\delta^{13}C_{org}$ of 4.6 ‰ towards the first peak of $\delta^{13}C_{org}$ with -24.2 ‰ at 103.22 m. The peak phase (between 103.22 and 99.51 m) shows first the

decrease towards the intermediate trough with a minimum of -26.7 ‰ at 101.6 m and the second peak with -24.3 ‰ at 99.80 m. The plateau phase (between 99.51 and 88.03 m) has a mean of -25.4 ±0.3 ‰. During the recovery phase (between 88.03 and 65.2 m) $\delta^{13}C_{org}$ values decrease by 3 ‰. The background level following the end of OAE2 between 65.2 m and the top of the recovered Cretaceous interval at 23.93 m is -28.2 ±0.2 ‰.

A comparable sequence of events is recorded in the $\delta^{13}C_{carbonate}$ dataset of OAE1a in La Bédoule (Fig. 3). The pre-OAE phase between 94.55 m and the top of interval C2 of Menegatti et al. (1998) at 76.87 m has a mean of 1.9 ±0.1 ‰. The precursor phase corresponding to stage C3 of Menegatti et al. (1998) and characterized by two prominent minima in $\delta^{13}C_{carbonate}$ of ~1.3 ‰ is between 76.87 and 70.91 m. The prominent increase of the OAE1a positive isotope excursion, identified as the onset phase, is identical with C4 and begins at the last minimum at 70.91 m and lasts until the first peak of 3.7 ‰ at 65.58 m. This interval is also characterized by a major lithological change at 68.09 m in the composite record of Cores LB3 and LB1 from limestones below to marlstones above (Fig. 3). This lithological change occurs 4 cm above a major increase in $\delta^{13}C_{carbonate}$ from 2.5 ‰ at 68.09 m to 3.0 ‰ at 68.05 m (Fig. S10), suggesting that the lithological change did not influence the increasing trend of $\delta^{13}C_{carbonate}$. The peak phase encompasses C5 and C6 and lasts until the end of the increase to 4.3 ‰ at 55.81 m. The adjacent plateau phase with an average of 4.3 ‰ (StDev 0.2 ‰) starts at 55.81 m and lasts until the boundary between C7 and C8 at 29.92 m. The following recovery phase between 29.92 and 10.75 m is identical with C8 of Menegatti et al. (1998). The background level of the post-OAE phase for the interval between 10.75 m and the top of the recovered cretaceous interval is 2.7 ±0.2 ‰.

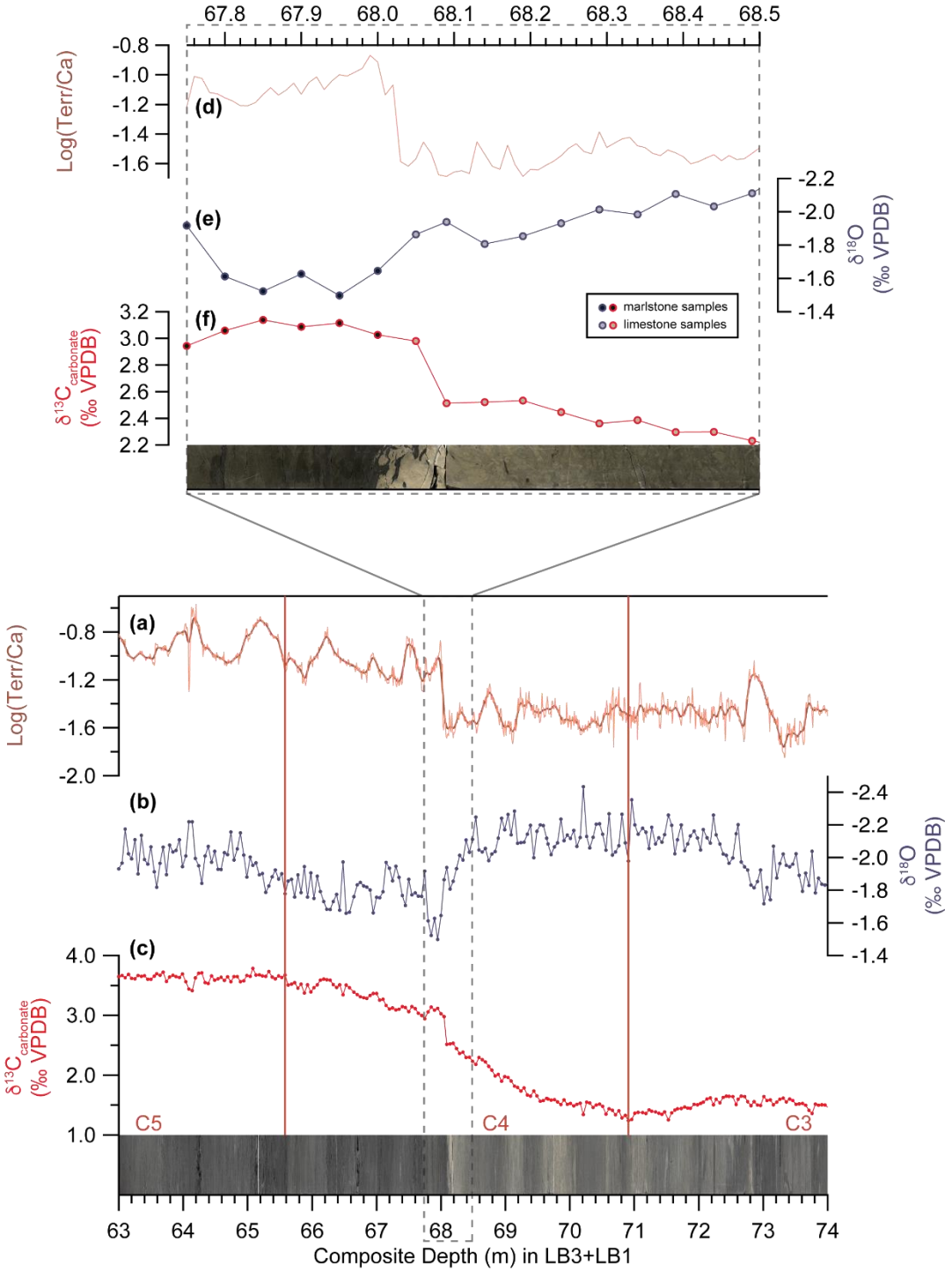

Fig. S10. $\delta^{13}C_{carbonate}$ increase during the onset of OAE1a and enlarged interval across the lithological change from limestone to marlstone dominated deposits. **(a)** and **(d)** Log(Terr/Ca). **(b)** and **(e)** d18O. **(c)** and **(f)** d13C. Stable Isotope data are from Lorenzen et al. (2013) with new high-resolution isotope data from this study. Note the depth difference between the increase in $\delta^{13}C$ in comparison to the decrease in carbonate content shown in core photos and Log(Terr/Ca).

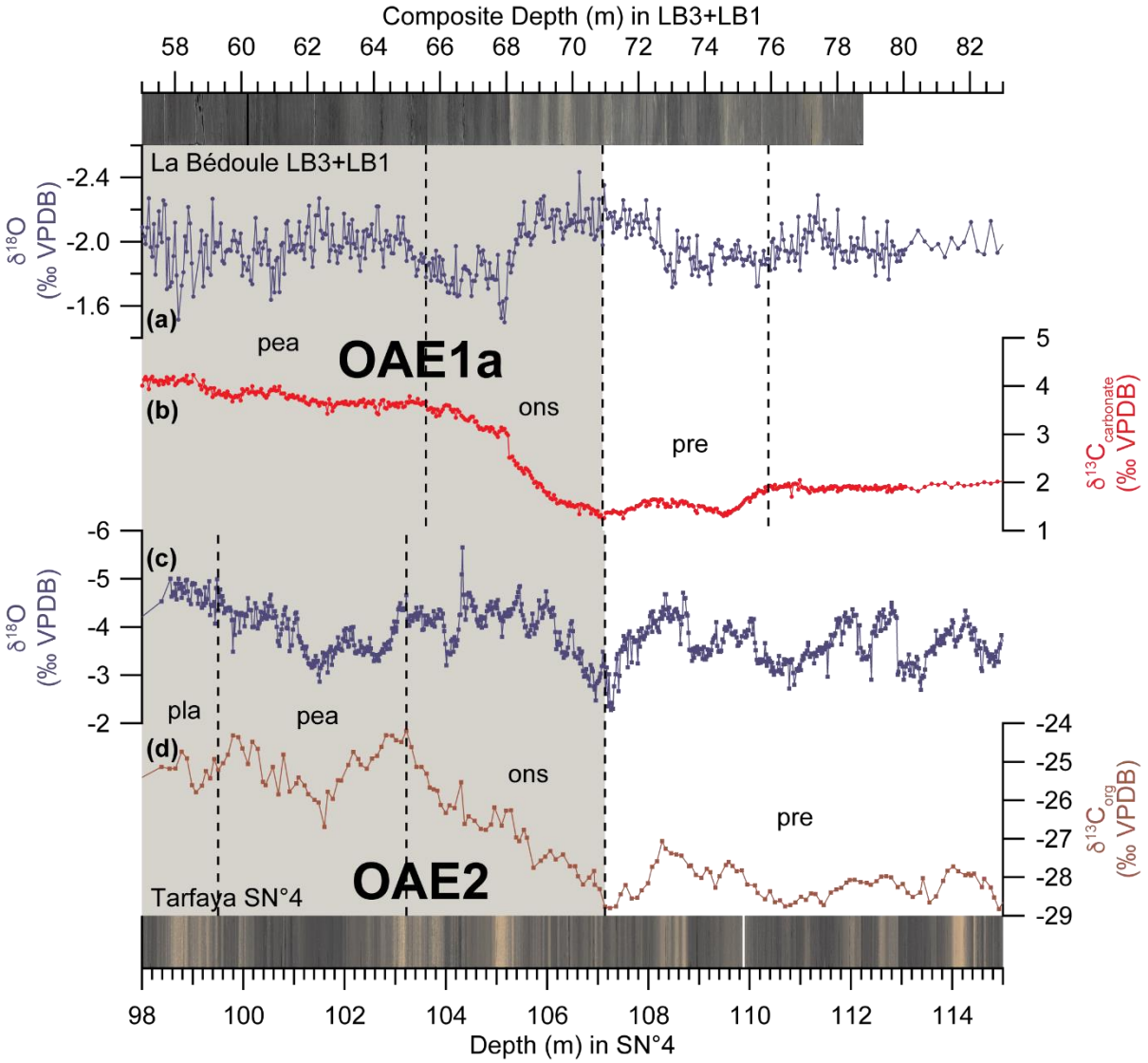

Fig. S11. Stable Isotopes records of LB3/LB1 and SN°4 during the early phases of OAE1a and OAE2. **(a)** $\delta^{18}O$ and **(b)** $\delta^{13}C_{carbonate}$ for OAE1a from Lorenzen et al. (2013) with new high-resolution isotope data from this study. **(c)** $\delta^{18}O$ and **(d)** $\delta^{13}C_{org}$ for OAE2 from Kuhnt et al. (2017) and Beil et al. (2018). The phases of OAE1a and OAE2 are indicated as vertical black dashed lines and marked with the abbreviations for precursor (pre), onset (ons), peak (pea), plateau (pla) and recovery (rec) phase.

Supplementary Material S12 -Segmentation of the NGR-record of LB3/LB1 for OAE1a

The uppermost segment N1 extends from 34.22 to 0 m and is characterized by strong cyclicity with wavelengths between 1.5 and 2.5 m and amplitudes predominantly larger than 15 cps. EHA-analysis shows a prominent signal at 1.1 m (0.88 m^{-1})

consistent over the entire interval. A second strong wavelength is detected at 2.2 m (0.45 cycles/m) between 17 and 6 m. The downcore NGR-record of segment N2 between 59.42 and 34.22 m shows a decreasing amplitude of short wavelength (0.5 – 2.5 m) cycles from >15 to <10 cps. EHA-analysis reveals a wider range of strong frequencies with the strongest cyclicities detected at wavelengths of 2.5 m (0.4 m^{-1}) and 0.8 m (1.2 m^{-1}). The NGR-record of segment N3 from 65.57 to 59.42 m shows 5 cycles with wavelengths between 0.8 and 1.8 m. EHA-analysis is influenced by signals from adjacent segments due to the window size of 6 m, but reveals a high amplitude signal at 1.6 m (0.63 m^{-1}). The NGR-curve of segment N4 between 87.32 and 65.57 m shows low amplitude (<7 cps), low wavelength (<1 m) cycles overprinted by long wavelength variability (>5 m). A cyclic imprint is detected by EHA-analysis within the wider range of 0.1 to 2.2 m^{-1} with a strong signal of 5.6 m wavelengths (0.18 m^{-1}) and weaker signals centred around 0.7 m (1.5 m^{-1}) and 0.5 m (2 m^{-1}). The lowest segment N5 between 105.84 m and 87.32 m shows an extended maximum between 92.67 and 89.17 m with maxima at ~35.5 cps. This interval is otherwise dominated by shorter wavelengths variability (<5 m) with an amplitude of <10 cps. EHA-analysis reveals stronger frequencies in the wavelengths band 1.2 – 7.2 m (0.14 – 0.85 m^{-1}).

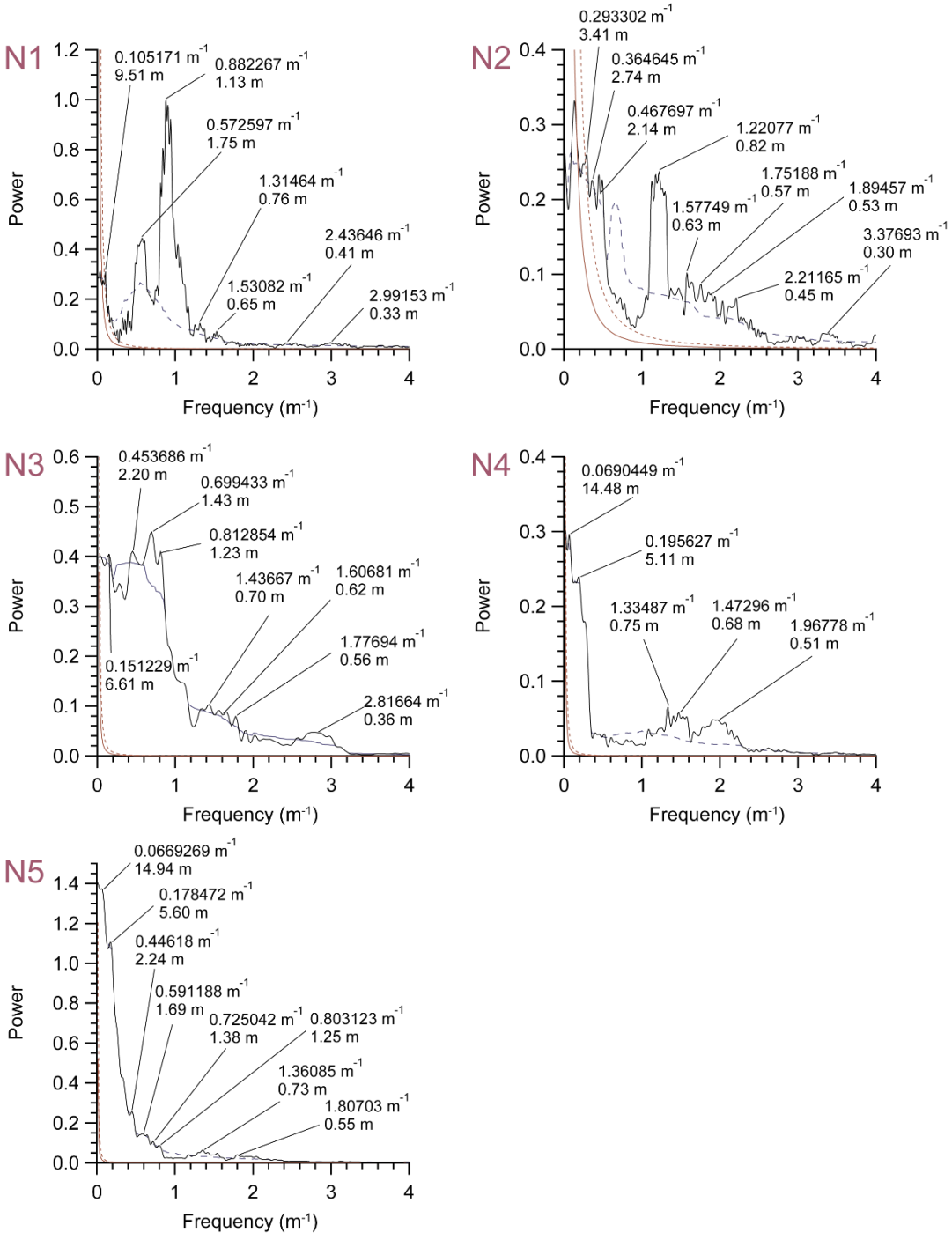

Fig. S13. Power spectra of NGR for specific depth segments in Core LB3/LB1: **N1** 0-34.22 m, **N2** 34.22-59.42 m, **N3** 59.42-65.57 m, **N4** 65.57-87.32 m and **N5** 87.32-105.84 m. Red lines indicate red noise level (solid) and 99 % confidence level (dashed). Multitaper method spectral analysis performed with the function *mtm* (Thomson, 1982) of the R-package *astrochron* (Meyers, 2014). Identified main frequencies are marked with frequency and wavelengths.

Table S14. Major identified frequencies in the NGR-record of Core LB3/LB1 and correlation to orbital frequencies for the Aptian interval from Laskar et al. (2004, 2011a).

N1			N2			N3			N4		
0-34.22 m			34.22-59.42 m			59.42-65.57 m			65.57-87.32 m		
frequency (m^{-1})	Wavelength (m)	correlated orbital cycle	frequency (m^{-1})	wavelength (m)	correlated orbital cycle	frequency (m^{-1})	wavelength (m)	correlated orbital cycle	frequency (m^{-1})	wavelength (m)	correlated orbital cycle
0.1052	9.51	e1	0.2933	3.41		0.1512	6.61	e1	0.0690	14.48	
0.5726	1.75		0.3646	2.74		0.4537	2.20	(e2)	0.1956	5.11	e1
0.8823	1.13	o2	0.4677	2.14	e2	0.6994	1.43	e3	1.3349	0.75	
1.3146	0.76		1.2208	0.82	o1	0.8129	1.23		1.4730	0.68	o1
1.5308	0.65	p1	1.5775	0.63	o2	1.4367	0.70	o1	1.9678	0.51	o2
2.4365	0.41	(p2)	1.7519	0.57		1.6068	0.62				
2.9915	0.33		1.8946	0.53		1.7769	0.56	o2			
			2.2117	0.45		2.8167	0.36	(p1)			
			3.3769	0.30	p2						
mean sedimentation rate (cm kyr^{-1}):		3.07	mean sedimentation rate (cm kyr^{-1}):		1.74	mean sedimentation rate (cm kyr^{-1}):		1.50	mean sedimentation rate (cm kyr^{-1}):		1.37

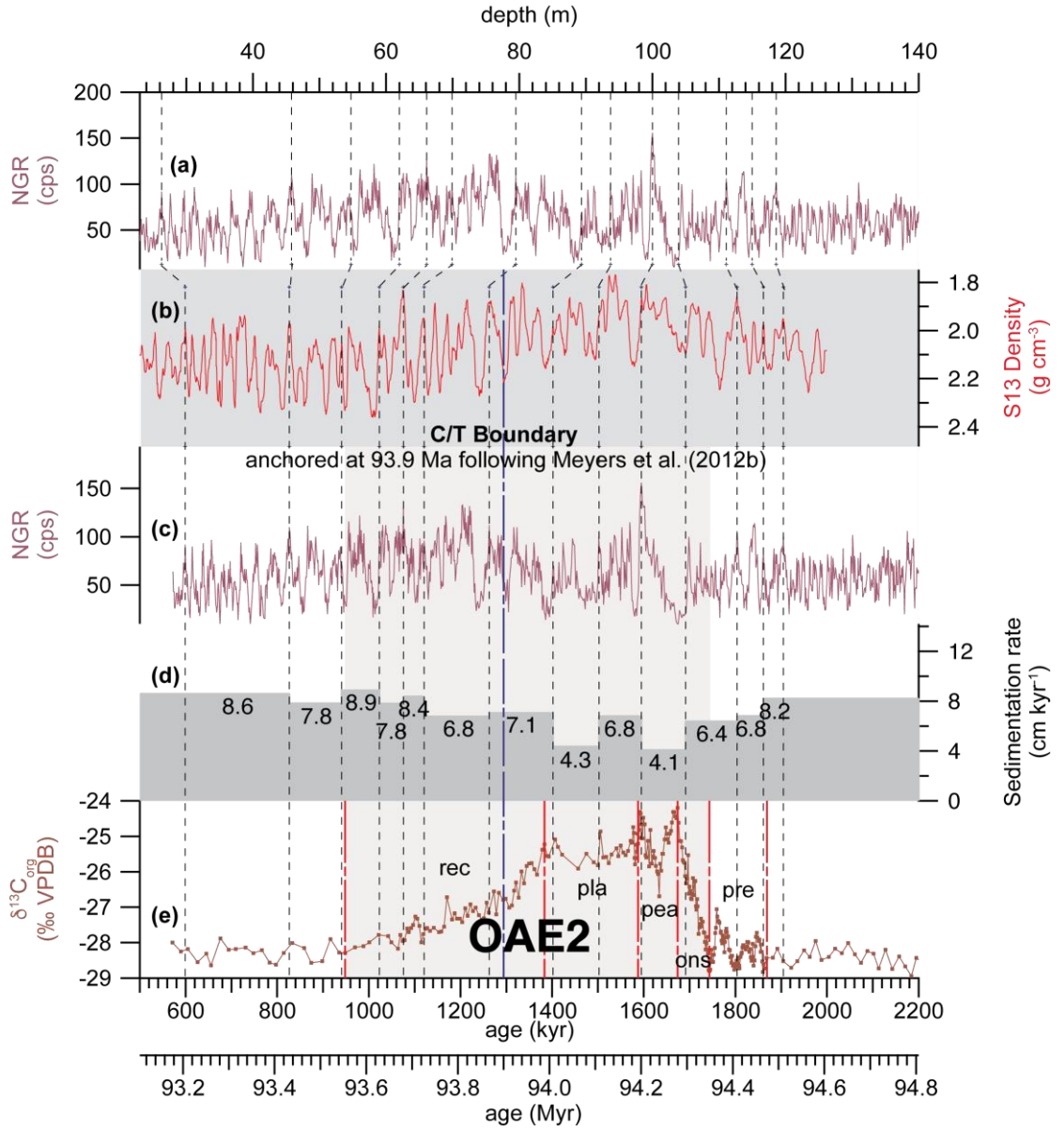

Fig. S15. Age tuning of Core SN°4. **(a)** NGR record of Core SN°4 on depth scale (top). **(b)** Target density curve from Meyers et al. 2012a highlighted in light grey. **(c)** NGR record of Core SN°4 on time scale (bottom). **(d)** Sedimentation rates. **(e)** $\delta^{13}C_{org}$ with phases of OAE2 indicated by vertical red lines and abbreviations for precursor (pre), onset (ons), peak (pea), plateau (pla) and recovery (rec) phase. Vertical, grey, dashed lines indicate tie points. The C/T-boundary is indicated by the blue dashed line.

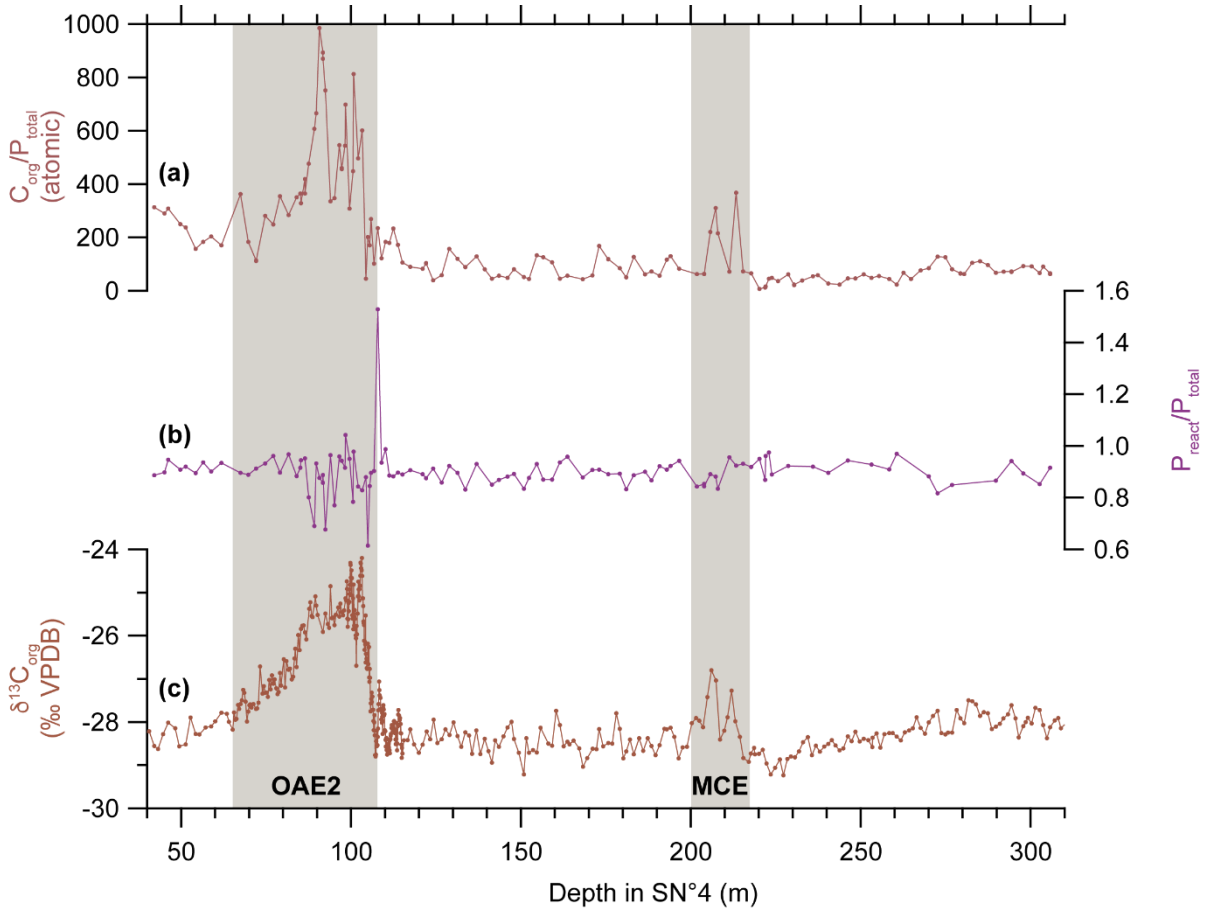

Fig. S16. Phosphorus ratios in Core SN°4. **(a)** C_{org}/P_{total}. **(b)** P_{react}/P_{total}. **(c)** $\delta^{13}C_{org}$ from Kuhnt et al. (2017) and Beil et al. (2018).

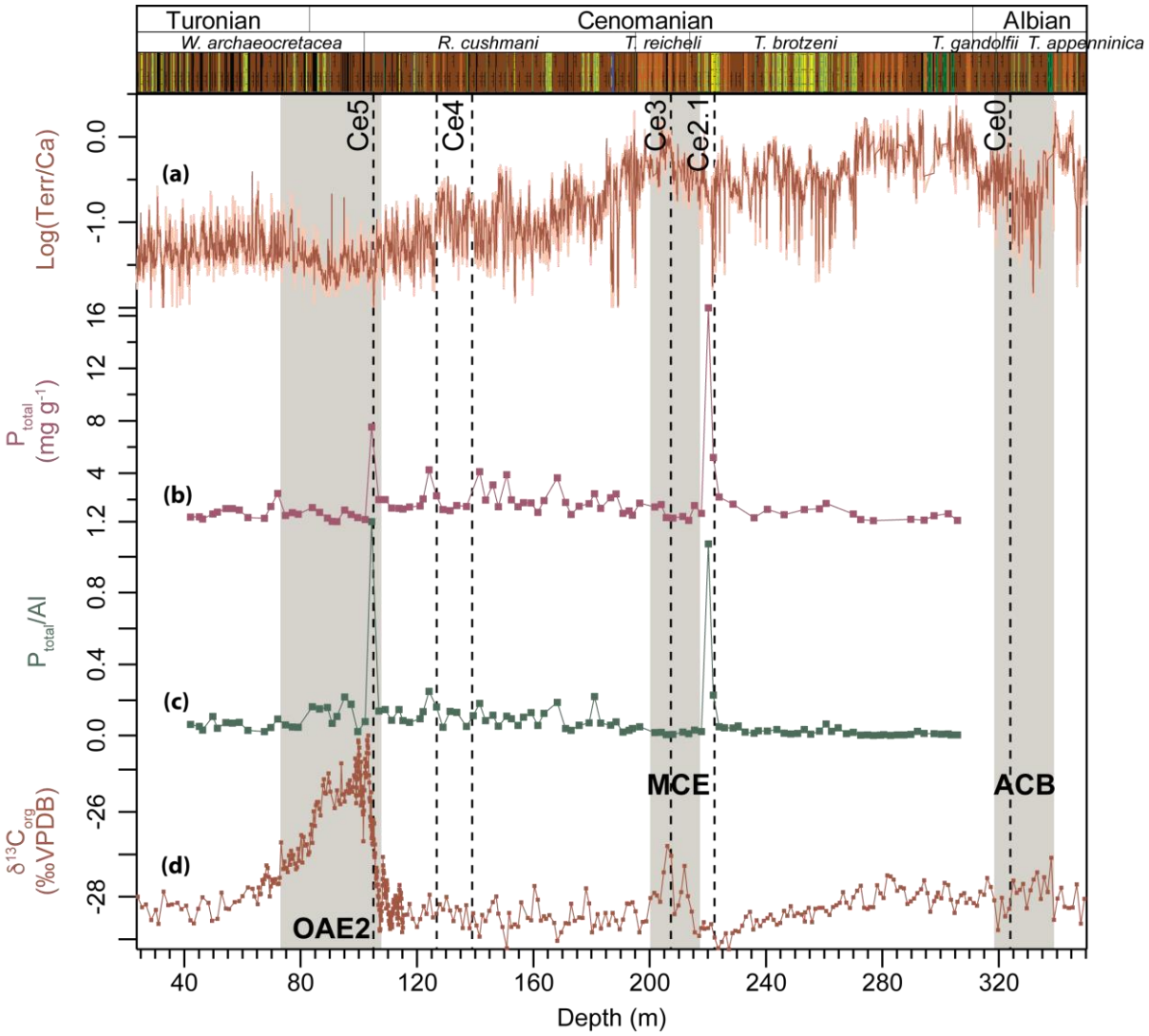

Fig. S17. Sea level reconstruction and phosphorus concentrations in Core SN°4. **(a)** XRF-scanning derived Log(Terr/Ca) and sea level correlation of Beil et al. (2018) to the regional reconstruction of Kuhnt et al. (2009). **(b)** Total phosphorus concentrations (P_{total}) and **(c)** ratio of P_{total} to aluminium. **(d)** $\delta^{13}C_{org}$ from Kuhnt et al. (2017) and Beil et al. (2018). Grey vertical bars indicate the carbon isotope excursions Albian-Cenomanian boundary event (ACB), mid-Cenomanian event (MCE) and Oceanic Anoxic Event 2 (OAE2). Vertical dashed lines and abbreviations on top indicate transgressive surfaces of Cenomanian sea level cycles.

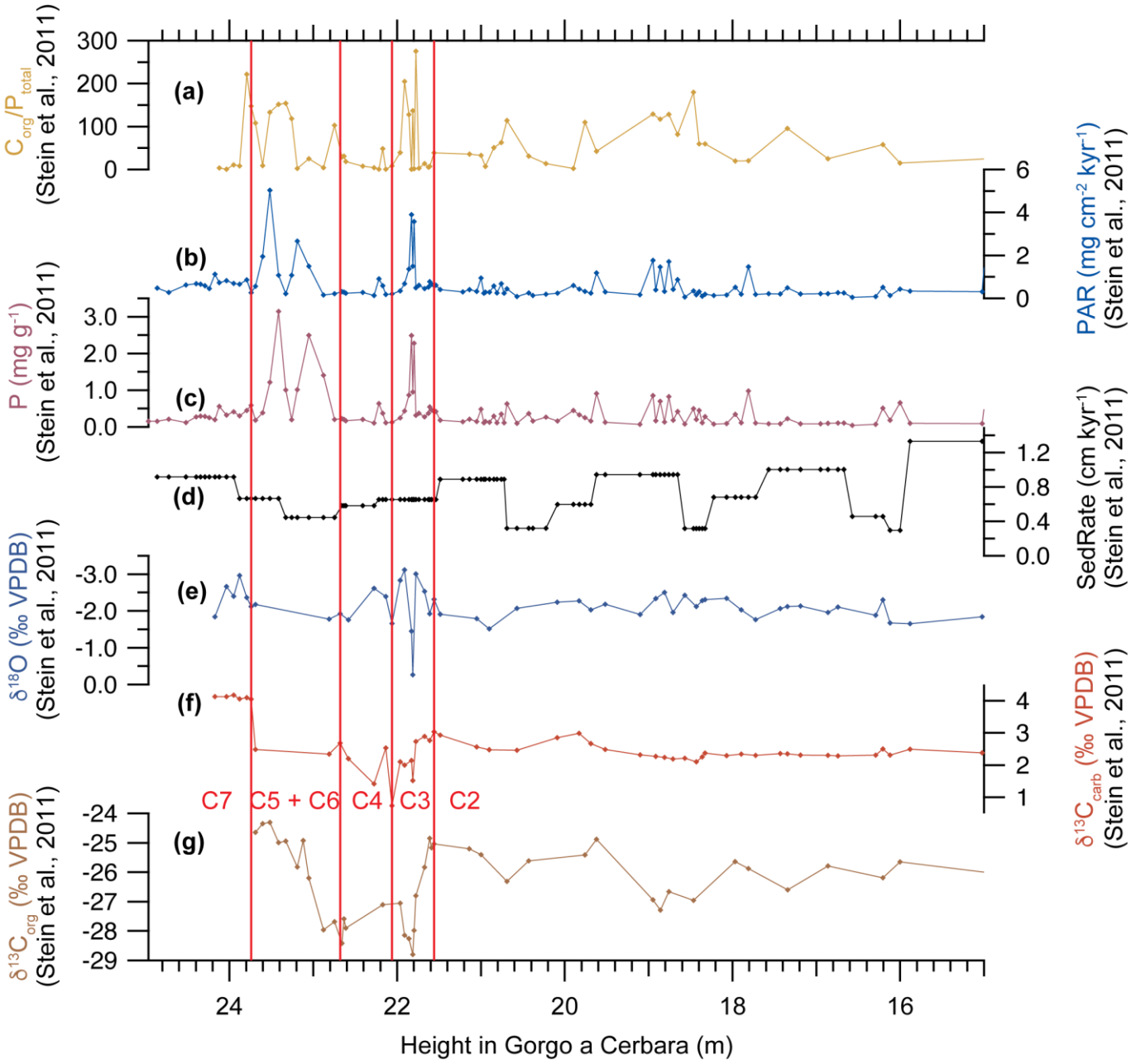

Fig. S18. Phosphorus and stable isotope data for the early interval of OAE1a from Stein et al. (2011). **(a)** C_{org}/P_{total}. **(b)** Phosphorus accumulation rate (PAR). **(c)** Phosphorus concentration. **(d)** Sedimentation rate (SedRate). **(e)** $\delta^{18}O$. **(f)** $\delta^{13}C_{carb}$. **(g)** $\delta^{13}C_{org}$.